

Scalar Spin Chiral Order via Bond Selectivity in Strained Collinear Ferrimagnets

Xin Liu, Li Ma*, Mingyue Zhao, Shun Niu, Yu Liu, Yang Li, Jiayao Zhu, Yiwen Zhang

Fengxian Ma, Dewei Zhao, Guoke Li, Congmian Zhen, Denglu Hou

Hebei Key Laboratory of Photophysics Research and Application, College of Physics, Hebei Normal University, Shijiazhuang, 050024, China.

Abstract

Scalar spin chirality (SSC) drives a series of topological transports in noncoplanar magnets. However, the ordering temperature of magnet hosting intrinsic SSC order is typically below 100 K. Current approaches to achieve near-room-temperature SSC order largely rely on external fields or chemical doping in noncollinear magnets. A significant challenge persists in generating and controlling SSC order in high-temperature collinear magnets. Here, using the collinear ferrimagnet Mn_4N with Néel temperature $T_N \sim 740$ K as a platform, we demonstrate that isotropic strain acts as a clean and continuous tuning parameter to induce long-range SSC order by first-principles calculations. As strain increases from -1.33% to 2.66% , the magnetic ground state evolves continuously from a collinear to a noncoplanar configuration, activating the SSC order and enhancing its magnitude from zero to ~ 2.32 . Our quantitative orbital-resolved bonding analysis reveals that strain selectively suppresses the bond between Mn $3d$ orbitals and N $2p$ orbitals, driving dual prerequisites for the SSC order. Specifically, the decreased covalent spin-pairing activates Mn $3c$ moments within the (111) plane, simultaneously the suppressed N-mediated ferromagnetic superexchange interaction shifts the balance of the nearest-neighbor Mn $3c$ sites toward antiferromagnetic exchange interaction. Our findings establish a powerful strain mediated route to construct the SSC order in high temperature collinear magnets.

Introduction

A series of novel physical phenomena in noncoplanar magnets has been observed, including the topological Hall effect¹⁻⁴, anomalous Hall effect⁵⁻⁷, topological Nernst effect⁸, thermal Hall effect^{9,10}, higher-order harmonics of the planar Hall effect¹¹ and spin splitting¹². To quantitatively characterize the degree of non-coplanarity, scalar spin chirality (SSC) has been introduced, defined as $\mathbf{S}_i \cdot (\mathbf{S}_j \times \mathbf{S}_k)$, where \mathbf{S}_α ($\alpha = i, j, k$) represent the localized spins of three nearest neighbor sites. The origins of these physical phenomena can be mainly attributed to the following mechanisms: SSC fluctuations^{10,13,14}, SSC induced skew scattering^{9,15,16}, and intrinsic contributions by SSC order^{1,3,5}. Theoretical studies further predict that SSC order would also induce phenomena such as the quantum anomalous Hall effect¹⁷⁻²⁰, quantum topological Hall effect^{20,21}, topological magneto-optical Kerr effect²², and quantum topological magneto-optical Kerr effect²². Intrinsic SSC order is relatively rare in magnetic materials, partly because it is canceled out by lattice symmetry.²³ Currently reported systems with SSC order have mostly low ordering temperatures (below 100 K), as shown in Table 1. Currently, largely efforts are being directed toward the construction and control of SSC order near-room-temperature. Existing strategies involve using external fields^{7,14,24-27} or chemical doping²⁸⁻³¹ to modulate the ground-state magnetic configuration in noncollinear antiferromagnets. In this context, it is worth considering whether the above strategy can be extended to collinear systems with antiferromagnetic (AFM) exchange interaction. To this end, Mn₄N is selected as the research platform in this work for the following reasons. AFM interaction between magnetic Mn atoms exists in collinear Mn₄N with a high Néel temperature of ~740 K.³² Besides, Mn atoms

form a frustrated triangular lattice supporting complex spin orders.³³ Here, strain is used as a control parameter, owing to its clean and highly tunable nature.

Table 1. List of materials hosting scalar spin chirality (SSC) order. We group the materials into two archetypes based on the SSC origin: inherent and induced. We also list the induced approach of SSC. Next, we list the magnetic materials platform and temperature of the experiments (T). Finally, we list the magnetic lattice type.

SSC Origin	Induced Approach	Materials	T (K)	Magnetic Lattice
inherent	—	$\text{CoNb}_3\text{S}_6^3$	~ 28	triangular
		$\text{CoTa}_3\text{S}_6^3$	~ 24	triangular
		MnTe_2^{12}	~ 86.5	triangular
		UCu_5^6	~ 1.2	triangular
		$\text{Nd}_2\text{Mo}_2\text{O}_7^1$	~ 40	pyrochlore
		$\text{Pr}_2\text{Ir}_2\text{O}_7^{5,34}$	~ 40	pyrochlore
		$\text{Nd}_2\text{Ir}_2\text{O}_7^{11}$	~ 30	pyrochlore
		$\text{Mn}_3\text{Sn}^{35}$	~ 50	kagome
induced	chemical doping	$\text{Mn}_{3-\delta}\text{Fe}_\delta\text{Sn}^{28}$	~ 300	kagome
		$\text{Fe}_{1+\delta}\text{Sb}^{30}$	~ 30	triangular
		$\text{Mn}_{3+\delta}\text{Ni}_{1-\delta}\text{N}^{29}$	~ 228	kagome
		$(\text{Y}_{1-x-y}\text{Tb}_x\text{Cd}_y)_2\text{Mo}_2\text{O}_7^{31}$	~ 20	pyrochlore
	magnetic field	PdCrO_2^2	~ 20	triangular
		$\text{Mn}_3\text{Sn}^{27}$	~ 350	kagome
		Mn_3Pt^7	~ 340	kagome
pressure	$\text{Mn}_3\text{Ge}^{24}$	~ 300	kagome	

In this work, we demonstrate that isotropic strain serves as a clean and continuous tuning parameter to induce SSC order in the high-temperature collinear ferrimagnet Mn_4N . As strain varies from -1.33% to 2.66% , the magnetic ground state continuously evolves from a collinear configuration to a noncoplanar state, thereby

activating the SSC order and amplifying its magnitude from zero to approximately 2.32. Through first-principles analysis, we reveal that this phase transition is governed by a strain-modulated bond selectivity. Rather than a simple geometric lattice expansion, tensile strain selectively suppresses Mn-N covalent bonds while preserving Mn-Mn covalent bonds. We demonstrate that this bond-selective suppression triggers a dual modulation: it activates the magnetic moments within the (111) plane and suppresses the ferromagnetic superexchange interaction, thereby stabilizing the SSC order. Ultimately, our work establishes a powerful, clean route to design topological spin structures directly within high-temperature collinear magnets.

A. Strain-induced Scalar Spin Chiral Order

The crystal structure of Mn_4N is illustrated in Fig. 1a. This compound crystallizes in the cubic space group $Pm\bar{3}m$ (No. 221). The Mn atoms at the corner sites are denoted as Mn1a (corresponding to Mn1), those at the face-center sites as Mn3c (corresponding to Mn2, Mn3, Mn4), and the body-center site is occupied by N atoms. Based on experimental³⁶⁻³⁸ and theoretical calculations^{37,39-41}, both collinear and noncoplanar ferrimagnetic configurations have been reported for the unstrained Mn_4N . In the collinear ferrimagnetic configuration, the spins of the Mn1a and Mn3c intra-sublattices are parallel, while the spins of the Mn1a and Mn3c inter-sublattices are antiparallel, which is the case in Fig. 1b where $\theta=180^\circ$. In the noncoplanar ferrimagnetic configuration, the spins of the four Mn inter-sublattices are no longer collinear but noncoplanar, the angle between them is 110° , as shown in Fig. 1b where $\theta=110^\circ$. To investigate the effect of strain on spin configuration, a zero-strain point was first defined, which corresponds to the equilibrium lattice parameter

$a = b = c = 3.75 \text{ \AA}$ of Mn_4N obtained by DFT calculation.

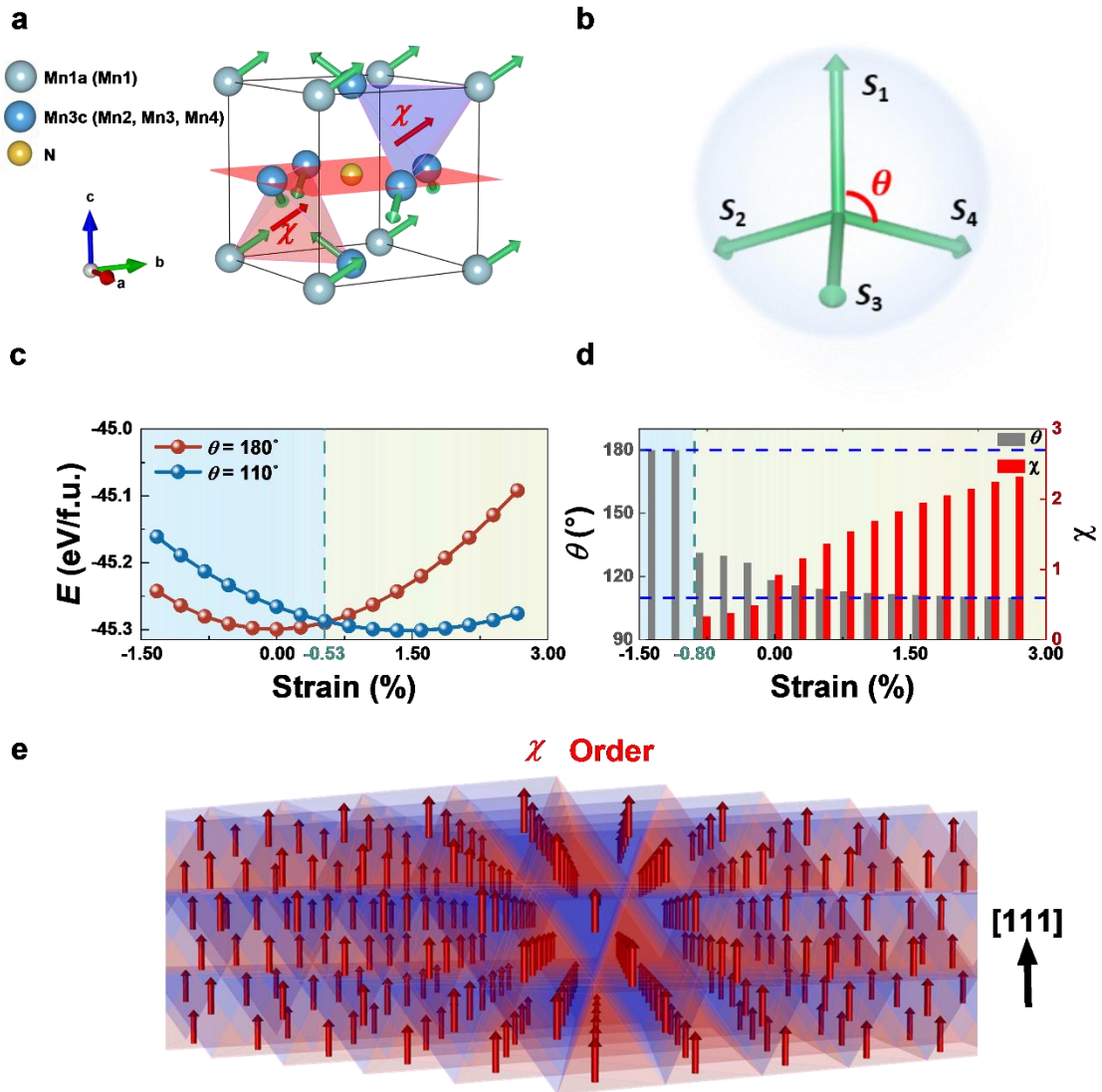


Figure 1 Strain-induced magnetic phase transition and the emergence of scalar spin chirality order in Mn_4N . **a** Magnetic and crystal structures of Mn_4N . There are only two types of magnetic tetrahedra in the lattice: red and blue. The green and red arrows represent the spin direction in the lattice and the direction of the total scalar spin chirality χ in each tetrahedron, respectively. **b** Schematic of a single tetrahedron of Mn atoms, which consists of four spin vectors S_α ($\alpha = 1, 2, 3, 4$). Here $\alpha = 1$ and $\alpha = 2, 3, 4$ indicate the corresponding spin orientation S_α at the Mn1a site and the Mn3c site, respectively. θ is the angle between the spins of the Mn1a site and the

Mn3c site. **c** Energy dependence on strain at $\theta = 110^\circ$ and $\theta = 180^\circ$. **d** Dependence of χ and θ on strain under the magnetic ground state. **e** Schematic of the χ distribution between adjacent (111) lattice planes. The gray planes represent the (111) lattice planes.

Fig. 1c shows the energy dependence on strain constraining the spin directions to $\theta = 110^\circ$ and $\theta = 180^\circ$, respectively. Under compressive (negative) strain, the energy of the $\theta = 180^\circ$ configuration is always lower than that of the $\theta = 110^\circ$ configuration. Thus, system remains in a collinear ferrimagnetic state. When tensile (positive) strain is applied, the collinear ferrimagnetic state is still stable up to 0.53%, after that the energy difference between $\theta = 110^\circ$ and $\theta = 180^\circ$ becomes larger and the noncoplanar ferrimagnetic state would be stable more and more. As a result, the system would undergo a transition from the collinear state with $\chi = 0$ to a noncoplanar state with $\chi = 2.32$ during the process of increasing tensile strain. This unique strain-dependent magnetic switching enables on/off control of χ . The above calculations only consider the cases where θ is 110° and 180° . Therefore, further self-consistent calculations without imposing initial magnetic constraints to determine the magnetic ground states under different strains are needed. The resulting strain dependence of both the θ and χ for the magnetic ground state is summarized in Fig. 1d. As the strain decreases from 2.66% to -1.33%, the θ value continuously increases from 110° to 180° , and the noncoplanar ferrimagnetic state is maintained until the compressive strain is greater than -0.80%, after which the θ value remains in a 180° collinear ferrimagnetic state. As a result, the corresponding χ value continuously decreased from 2.39 to 0. This demonstrates that external strain provides engineering that can not only

effectively activate but also continuously regulate χ .

As shown in Fig. 1a, Mn₄N contains two types of magnetic tetrahedra: red and blue. When the system adopts the noncoplanar ferrimagnetic state, the χ direction of both red and blue tetrahedra is along the [111] crystal direction. Fig. 1e schematically illustrates the tetrahedral and χ arrangement within three adjacent (111) lattice planes. It can be seen that the χ formed by each magnetic tetrahedron is arranged along the crystal direction [111] as shown by the red arrows, thus establishing a long-range ordered state of χ similar to magnetic dipole ferromagnetic order. This scalar spin chirality order may give rise to a spontaneous Hall effect⁵, spontaneous topological Hall effect³, and related physical phenomena.

B. Dual Prerequisites for Scalar Spin Chiral Order

To understand the formation mechanism of noncoplanar ferrimagnetic states in Mn₄N, we analyzed spin-related Hamiltonians where only the Heisenberg exchange interaction and the Dzyaloshinskii–Moriya interaction influences the θ between spins. In the centrosymmetric Mn₄N system, the Dzyaloshinskii–Moriya interaction is symmetry-forbidden, the θ is governed predominantly by the Heisenberg exchange interaction, which is described by $J_{ij}\mathbf{S}_i \cdot \mathbf{S}_j$. Here, J_{ij} represents the exchange coupling constant, and \mathbf{S}_i and \mathbf{S}_j denote the local spin at i and j sites. We calculated the dependence of the Mn moments at the Mn1a and Mn3c sites and the nearest-neighbor Mn3c-Mn3c exchange coupling constant J on strain to quantify this interaction, as shown in Figs. 2a-c. The Mn moment at the Mn1a site remains nearly constant at $\sim 3.22 \mu_B$ under strain, whereas the Mn moment at the Mn3c site, which is

highly sensitive to strain, increases from $0.6 \mu_B$ to $2.3 \mu_B$ as strain varies from -1.33% to 2.66% . Under zero strain, our calculated value is $1.06 \mu_B/\text{f.u.}$, which is nearly the same as the neutron diffraction value ($1.10 \mu_B/\text{f.u.}$)³².

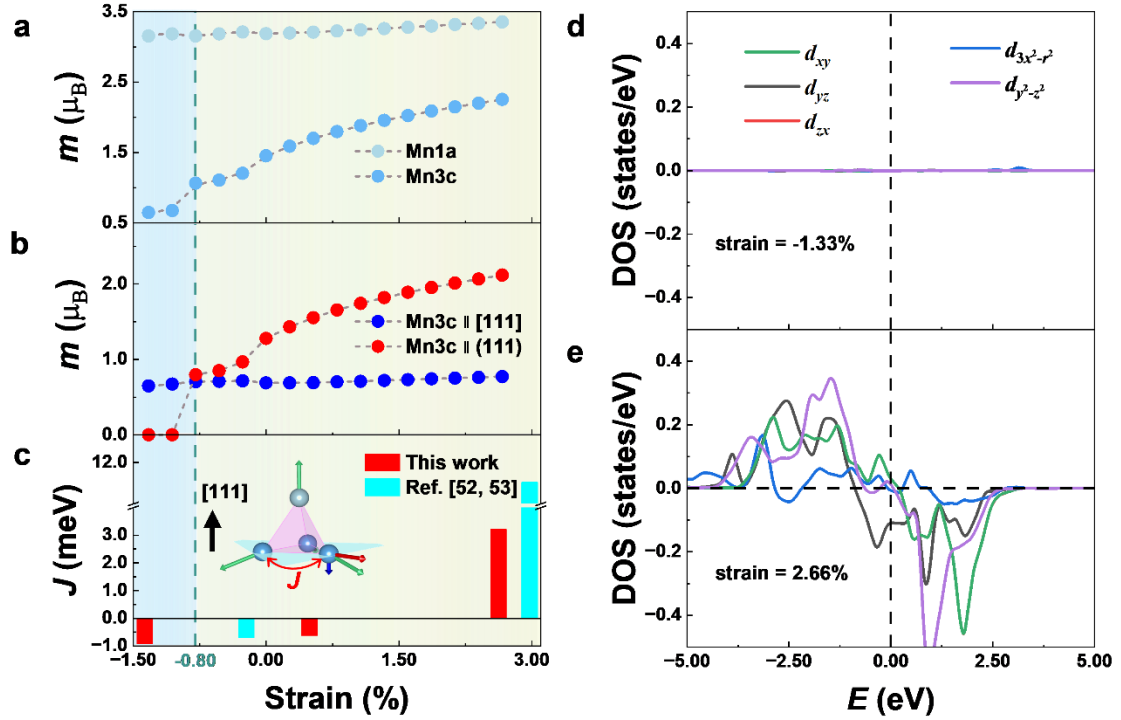


Figure 2. **Explore the requirements for the formation of scalar spin chiral order on local moments and exchange interactions.** **a** Strain dependence of the Mn moments at Mn1a and Mn3c sites. **b** Strain evolution of the Mn3c moment components: Mn3c||[111] (parallel to [111] crystal direction) and Mn3c||(111) (lying within the (111) lattice planes), corresponding to the blue and red arrow illustrated in the inset of (c), respectively. **c** Strain variation of the nearest-neighbor exchange coupling constant J between Mn3c sites. Projected density of states (PDOS) of the Mn3c 3d orbitals onto the (111) plane at strains of -1.33% (d) and 3.00% (e).

We note that the Mn3c moments exhibit a discontinuous change at the -0.80% strain point where the system underwent a magnetic transition from collinear to noncollinear. To further analyze the moment at Mn3c site, the total Mn moment at Mn3c

site is decomposed along two directions: parallel to the $[111]$ direction, denoted as $Mn3c \parallel [111]$ (blue arrow) which is parallel to Mn1a moment; and parallel to the (111) plane, denoted as $Mn3c \parallel (111)$ (red arrow) which is vertical to Mn1a moment, as shown in the inset of Fig. 2c.

Fig. 2b shows the strain dependence of $Mn3c \parallel [111]$ and $Mn3c \parallel (111)$. It is interesting to observe that the $Mn3c \parallel [111]$ component remains nearly constant at $\sim 3.22 \mu_B$ over the whole strain region, as the case of the Mn1a moment; whereas the $Mn3c \parallel (111)$ component begins to obtain a nonzero value just at -0.80% and continues to increase with the increase of the strain, similar to the scenario of χ in Fig. 1d. This indicates that the $Mn3c \parallel (111)$ moment is a key element in constituting the noncoplanar ferrimagnetic state, i.e., the χ order. At 2.66% strain, our calculated Mn3c moment ($2.31 \mu_B$) agrees well with that ($2.35 \mu_B$) of the reference⁴².

Since the $Mn3c \parallel (111)$ and Mn1a moments are mutually orthogonal, the formation of the χ order is dictated exclusively by the exchange interactions among the Mn3c sites within the Heisenberg model. In this context, the nearest-neighbor Mn3c-Mn3c exchange coupling constant J is shown in Fig. 2c at three representative strain points: the maximum compressive strain (-1.33%), the maximum tensile strain (2.66%), and the strain corresponding to the energy crossover point in Fig. 1c (0.53%). A clear evolution regarding J can be expected. As the strain changes from -1.33% to 2.66% , the net ferromagnetic exchange interaction between nearest-neighbor Mn3c sites weakens and eventually undergoes a sign reversal, transitioning into a strong antiferromagnetic exchange interaction. The calculated exchange coupling constant J evolves from -0.9 meV at -1.33% strain to -0.6 meV at 0.53% , and finally

reverses sign to 3.2 meV at 2.66% strain, confirming a strain-induced suppression of ferromagnetism and a transition toward antiferromagnetic coupling. As indicated by the cyan points in Fig. 2c, this trend is in excellent agreement with previously reported values at comparable lattice constants^{43,44}.

To understand the microscopic origin of this anomalous magnetic transition, we present the projected density of states (PDOS) of the Mn3c 3d orbitals onto the (111) plane at the representative strains of -1.33% and 2.66%, as shown in Figs. 2d, e. At a compressive strain of -1.33%, the in-plane PDOS contribution near the Fermi level is virtually zero. In stark contrast, under a tensile strain of 3.00%, a pronounced spin-polarized contribution strongly emerges across the *d* orbitals. This provides direct energy-space evidence for the orbitally-driven activation of the Mn3c||(111) moment.

Consequently, the prerequisite for the formation of χ order is the activation of the Mn3c||(111) moment and a sufficiently weak ferromagnetic exchange interaction (or even an antiferromagnetic exchange interaction) between the nearest-neighbor Mn3c sites.

C. Bond Selectivity of Strain and Mechanism of Scalar Spin Chiral Order

Since J is governed by the electron-orbital overlap, while the Mn3c||(111) moment is modulated by the chemical bond of the Mn3c orbitals, it is imperative to quantify the orbital responses to strain. Charge density difference (CDD) mapping quantitatively delineates the spatial redistribution of electrons, providing a direct visual representation of these orbital responses.

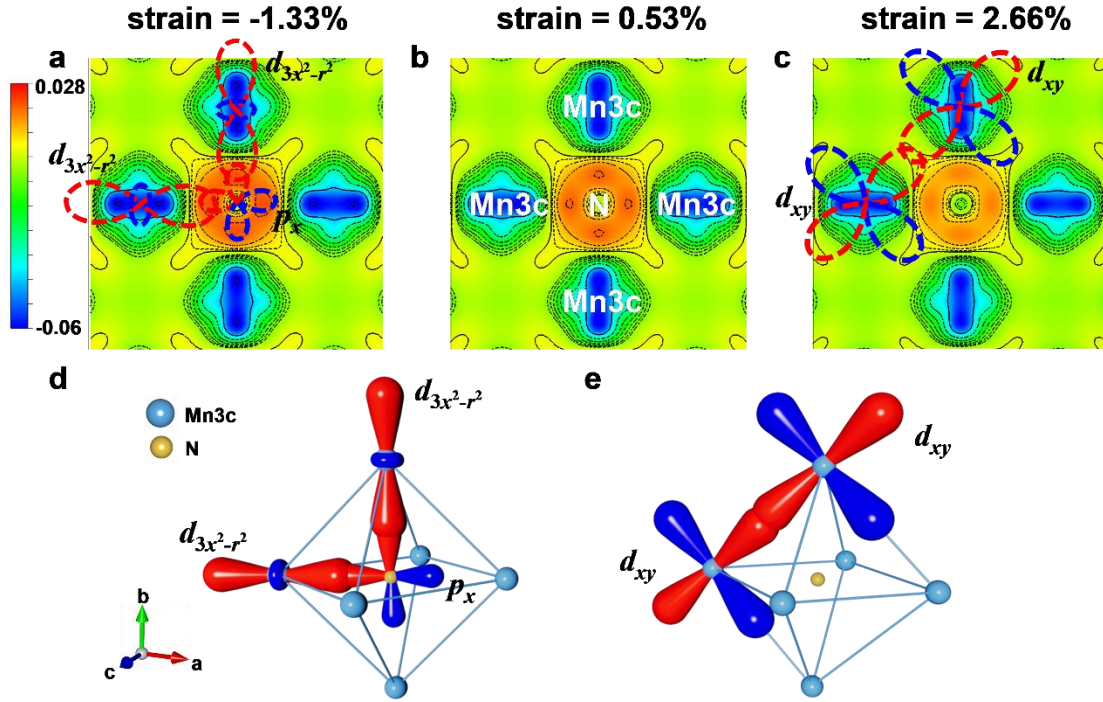


Figure 3. Two key orbital bonding between nearest-neighbor Mn3c sites in Mn₄N through charge density difference (CDD) analysis. CDD on the (001) lattice plane (corresponding to the red plane in Fig. 1a) under strains of -1.33% (a), 0.53% (b), and 2.66% (c). The red and blue areas represent electron accumulation and depletion, respectively. The isosurface levels are set to $-0.028 \text{ e}/\text{\AA}^3$ (red, positive) and $-0.06 \text{ e}/\text{\AA}^3$ (blue, negative). Black dashed lines indicate charge contour levels. The red and blue dashed loops delineate the projections of the Mn3c and N orbitals onto the (001) plane, serving as spatial references for orbital hybridization. Schematic representations of the two orbital bonding configurations deduced from the CDD maps. Schematics of the polar σ covalent bond formed by the hybridization of the Mn3c $d_{3x^2-r^2}$ ($d_{3y^2-r^2}$) orbital and the N p_x (p_y) orbital (d) and the nonpolar σ covalent bond between the d_{xy} orbitals of nearest-neighbor Mn3c atoms (e).

In order to reflect the changes in the charge density of each component atom in Mn₄N, we performed the following CDD calculation:

$$\text{CDD} = \rho_{\text{Mn}_4\text{N}} - \rho_{\text{Mn}_1} - \rho_{\text{Mn}_2} - \rho_{\text{Mn}_3} - \rho_{\text{Mn}_4} - \rho_{\text{N}} \quad (1)$$

where $\rho_{\text{Mn}_4\text{N}}$ represents the charge density of the complete unit cell, ρ_{Mn_α} ($\alpha = 1, 2, 3, 4$) and ρ_{N} correspond to the charge densities of isolated Mn_α and N atoms placed at their respective crystal positions, respectively.

Figs. 3a-c show the CDD distribution on the (001) lattice plane under representative strains of -1.33% , 0.53% , and 2.66% . In these maps, the red and blue regions denote electron accumulation and depletion, respectively, while the dashed loops delineate the projections of the Mn3c and N orbitals. There are two characteristics of the distribution of CDD. First, an obvious positive CDD along x and y axes suddenly appears between Mn3c site and N and is very close to the N atoms as indicated by the black contour lines in the red area, and an obvious negative CDD of the Mn3c atom only along x or y axis also appears at the same time as shown by the black contour line in the blue area. Thus, the CDD distribution is strongly anisotropic, and meets the characteristics of the $d_{3x^2-r^2}$ and $d_{3y^2-r^2}$ orbitals of Mn atoms and the p_x and p_y orbitals of N atoms. That is to say, the electrons in the $d_{3x^2-r^2}$ ($d_{3y^2-r^2}$) orbital of Mn3c atoms form polar covalent bonds with the electrons in the p_x (p_y) orbital of N atoms. To intuitively illustrate this specific orbital overlap configuration, a corresponding schematic is provided in Fig. 3d. Second, there is also a positive CDD (yellow area) between the nearest-neighbor Mn3c atoms, and its direction is 45 degrees to the coordinate axes, showing the anisotropy of the Mn3c d_{xy} orbitals. This is not a characteristic of metallic bonds, but rather of covalent bonds. The nonpolar σ covalent bond forming by the d_{xy} orbitals of the Mn3c atoms is explicitly illustrated in Fig. 3e, which is allowed whether from the perspective of energy or orbital direction.

As the tensile strain systematically increases from -1.33% to 2.66% , there are also two characteristics on the value of CDD. First, the value of CDD at the Mn3c $d_{3x^2-r^2}$ orbital and the N p_x orbital overlap is significantly decreased, reflecting a severe attenuation of the polar σ covalent bond. In stark contrast, the value of CDD between the overlapping d_{xy} orbitals of nearest-neighbor Mn3c sites remain virtually unchanged, implying that the nonpolar σ covalent bond is essentially insensitive to the strain.

While the CDD analysis offers an intuitive spatial perspective, a rigorous quantitative evaluation of the bonding interactions is urgently needed. To this end, we employed the projected crystal orbital Hamiltonian population method (pCOHP). This analytical technique mathematically extracts the specific bonding and antibonding contributions between selected atomic orbitals. A comprehensive analysis across all 36 conceivable orbital combinations confirms that the nearest-neighbor Mn3c interactions are predominantly governed by two distinct bonding pathways: the hybridization between the Mn3c $d_{3x^2-r^2}$ orbital and the N p_x orbital, and the direct overlap between the Mn3c d_{xy} orbital and the Mn3c d_{xy} orbital. This dual-pathway bonding model is perfectly consistent with the preceding CDD analysis. The corresponding energy-resolved profiles for these two dominant orbital interactions under different strains are presented in Figs. 4a-c. For both bonding mechanisms, the profiles remain positive below the Fermi level, signifying robust bonding states.

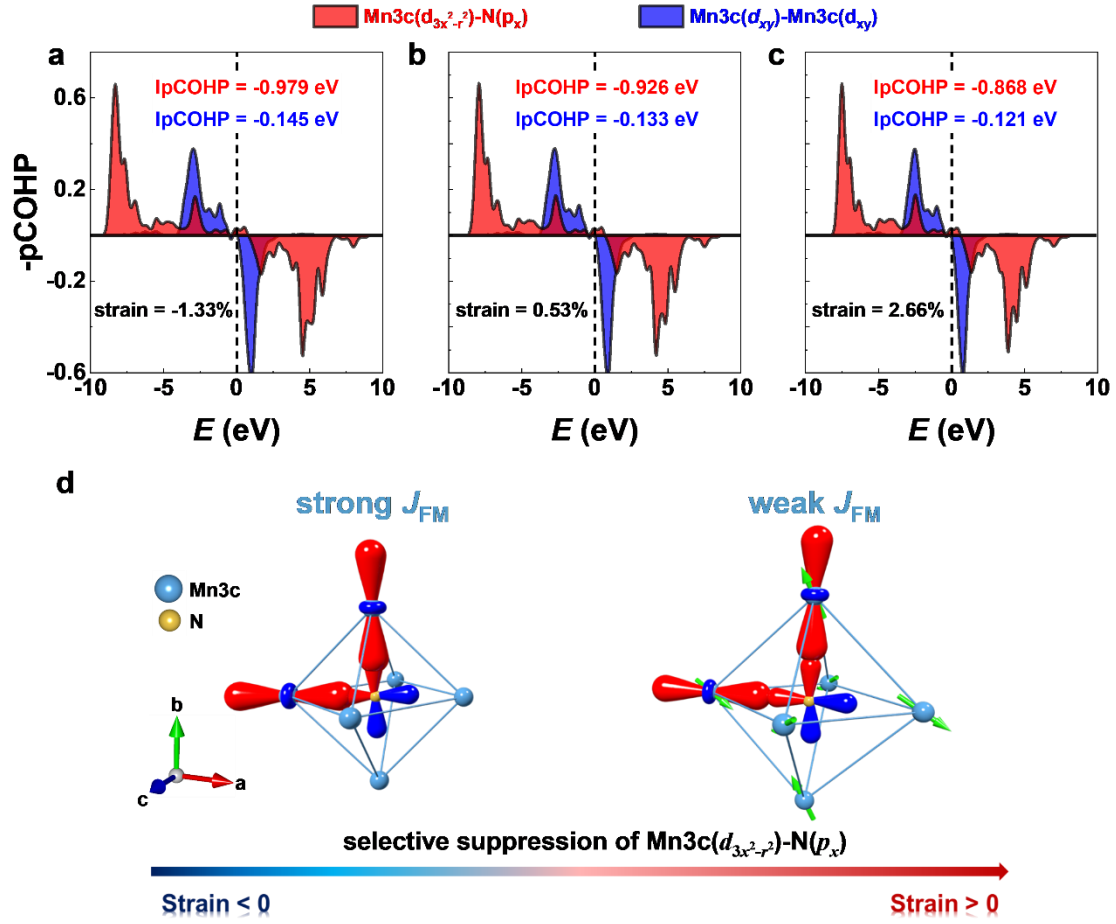


Figure 4. **Formation mechanism of the scalar spin chirality order via the quantitative orbital-resolved bonding analysis.** Projected crystal orbital Hamiltonian population (pCOHP) profiles for the two principal orbital interactions: the Mn3c $d_{3x^2-r^2}$ and N p_x bond (red curves), and the Mn3c d_{xy} and Mn3c d_{xy} bond (blue curves) under strains of -1.33% (a), 0.53% (b), and 2.66% (c). Positive and negative $-p\text{COHP}$ values denote bonding and antibonding characteristics, respectively. The red and blue text in each panel gives the integrated pCOHP (IpCOHP) values up to the Fermi level (measure of bond strength) of the Mn3c-N bond and the Mn3c-Mn3c bond, respectively. **d** Strain-dependent schematic of the dual modulation of the Mn3c || (111) moment and exchange interactions via bond-selective suppression. The left and right panels correspond to the covalent bond between the Mn3c $d_{3x^2-r^2}$ orbital and the N

p_x orbital and the magnetic configuration under the compressive and tensile strain conditions, respectively. The green arrows denote the activated Mn3c||(111) moments. J_{FM} represents the nitrogen-mediated ferromagnetic superexchange interaction of the nearest-neighbor Mn3c via the Mn3c ($d_{3x^2-r^2}$)-N (p_x) covalent bond.

The integrated projected crystal orbital Hamilton population (IpCOHP) parameter provides a measure of the bonding strength between two atoms.^{45,46} The more negative the parameter, the stronger the bonding interaction. We have calculated this IpCOHP up to the Fermi level to understand how changes in strains affect the two distinct bonding pathways. Specifically, the IpCOHP value for the hybridized Mn3c $d_{3x^2-r^2}$ orbital and N p_x orbital (the red text in each panel) progressively diminishes from -0.979 eV at -1.33% strain to -0.925 eV at 0.53% , and ultimately drops to -0.868 eV at 2.66% strain, with a total bond strength reduction of 0.111 eV. This systematic numerical reduction unequivocally demonstrates the pronounced suppression of this bonding channel, quantitatively confirming that the polar σ covalent bond is severely compromised under tensile strain. Conversely, the IpCOHP values for the overlapping d_{xy} orbitals between nearest-neighbor Mn3c sites decreased by only 0.024 eV throughout the strain range, remaining essentially unchanged. This quantitative stability is in perfect agreement with the strain insensitivity intuitively inferred from the CDD analysis. Quantitative IpCOHP analyses unveils a striking bond-selective response to the strain: strain strongly affects only the $d_{3x^2-r^2}$ orbital of Mn3c, while the d_{xy} orbital of Mn3c is largely unaffected.

Regarding the magnetic moment, the polar σ covalent bond formed by the Mn3c $d_{3x^2-r^2}$ orbital and N p_x orbital induces covalent spin-pairing, thereby suppressing the

local magnetic moment.⁴⁷ Under compressive strain in the left panel of Fig. 4d, the polar σ bond suppresses the local magnetic moment. This state is corroborated by the virtually zero in-plane density of states near the Fermi level shown in Fig. 2d. As the tensile strain increases, the strain exhibits bond selectivity. It selectively weakens the polar σ covalent bond, which mitigates covalent spin-pairing and activates the Mn3c || (111) moment indicated by the green arrows in the right panel of Fig. 4d. This activation corresponds to the spin polarization emerging in Fig. 2e. This evolution corresponds to Fig. 2b.

Regarding the exchange interaction, the nonpolar σ covalent bond between the d_{xy} orbitals of Mn3c sites establishes a direct exchange interaction pathway, favoring an antiferromagnetic exchange interaction J_{AFM} ,⁴⁸⁻⁵⁰ while the polar σ bond between the Mn3c $d_{3x^2-r^2}$ orbital and N p_x orbital establishes a 90° superexchange pathway, generating a ferromagnetic exchange interaction J_{FM} .⁴⁸⁻⁵⁰ The stronger the Mn3c-N (Mn3c-Mn3c) bond, the stronger the J_{FM} (J_{AFM}). When the strain varies from -1.33% to 2.66% , the Mn3c-N bond is selectively suppressed, resulting in the weakening of J_{FM} , as shown in Fig. 4d. During this process, the competition between the J_{AFM} and J_{FM} brings a new balance, leading to the exchange interaction J in Fig. 2c to change from ferromagnetic (negative) to antiferromagnetic (positive).

Now we discuss the experimental realization of these results. The scalar spin chirality order in Mn₄N can be introduced by epitaxially growing Mn₄N (111) films on tensile strain substrates such as MgO (111) or SrTiO₃ (111). Based on the influence of scalar spin chirality order in real and reciprocal space as discussed in the introduction, we expect unique transport features to emerge in such films, including

topological Hall effect (THE), anomalous Hall effect (AHE), and even in-plane anomalous Hall effect (IPAHE).

Conclusion

In summary, we investigated the strain-dependent magnetic responses of the collinear ferrimagnet Mn_4N using first-principles calculations. We find that the isotropic tensile strain drives the magnetic ground state from a collinear to a noncoplanar configuration, inducing a scalar spin chirality (SSC) order. The formation of the SSC order requires two prerequisites. One is the activation of $\text{Mn}3c$ moment in the (111) plane $\text{Mn}3c \parallel (111)$, and the other is a sufficiently weak ferromagnetic exchange interaction (or even an antiferromagnetic exchange interaction) between the nearest-neighbor $\text{Mn}3c$ sites. Electronic structure analyses including charge density difference and projected crystal orbital Hamiltonian populations reveal that tensile strain selectively suppresses the polar $\text{Mn}3c\text{-N}$ covalent bond. As a result, covalent spin-pairing is mitigated to activate $\text{Mn}3c \parallel (111)$ moment and the ferromagnetic superexchange interaction is weakened, ultimately stabilizing the SSC order. We propose that this bond-centric computational framework may also be applicable to inducing SSC order in other collinear ferrimagnets. Our findings work provides a new route for constructing SSC order.

Calculation Method

All first-principles calculations were performed within the framework of density functional theory (DFT) utilizing the Vienna Ab Initio Simulation Package (VASP)⁵¹⁻⁵³. The interactions between core electrons and valence ions were described using the projector-augmented wave (PAW) method. For the exchange-correlation functional, the

generalized gradient approximation (GGA) parameterized by the Perdew-Burke-Ernzerhof (PBE) formalism was adopted. A plane-wave energy cutoff of 520 eV and a Γ -centered $12 \times 12 \times 12$ k -point mesh for Brillouin zone sampling were used. The convergence criteria for the electronic self-consistent field and ionic relaxation were strictly set to 10^{-6} eV/cell and 10^{-3} eV/cell, respectively. Crucially, spin-orbit coupling (SOC) was explicitly incorporated in all static electronic structure calculations based on the fully relaxed crystal structures. To quantify the magnetic interactions, the DFT energies were mapped onto a classical Heisenberg spin model. Considering the exchange coupling constant J_{12} between spin points 1 and 2, the spin Hamiltonian⁵⁴ can be expressed as:

$$E_{\text{spin}} = J_{12} \mathbf{S}_1 \cdot \mathbf{S}_2 + \mathbf{S}_1 \cdot \mathbf{K}_1 + \mathbf{S}_2 \cdot \mathbf{K}_2 + E_{\text{other}} \quad (2)$$

where $\mathbf{K}_1 = \sum_{i \neq 1,2} J_{1i} \mathbf{S}_i$, $\mathbf{K}_2 = \sum_{i \neq 1,2} J_{2i} \mathbf{S}_i$, $E_{\text{other}} = \sum_{i,j \neq 1,2} J_{ij} \mathbf{S}_i \cdot \mathbf{S}_j$ where \mathbf{K}_1 , \mathbf{K}_2 and E_{other} do not depend on the spin directions of positions 1 and 2. Four collinear spin states are considered: (1) $\mathbf{S}_1 = S$, $\mathbf{S}_2 = S$, (2) $\mathbf{S}_1 = S$, $\mathbf{S}_2 = -S$, (3) $\mathbf{S}_1 = -S$, $\mathbf{S}_2 = S$, (4) $\mathbf{S}_1 = -S$, $\mathbf{S}_2 = -S$. These four states have the following energy expressions:

$$\begin{aligned} E_1 &= E_0 + E_{\text{other}} + J_{12} S^2 + K_1 S + K_2 S \\ E_2 &= E_0 + E_{\text{other}} - J_{12} S^2 + K_1 S - K_2 S \\ E_3 &= E_0 + E_{\text{other}} - J_{12} S^2 - K_1 S + K_2 S \\ E_4 &= E_0 + E_{\text{other}} + J_{12} S^2 - K_1 S - K_2 S \end{aligned} \quad (3)$$

Then J_{12} can be written as:

$$J_{12} = \frac{E_1 + E_4 - E_2 - E_3}{4S_1 S_2} \quad (4)$$

From this, the exchange coupling constant J_{12} , which governs the interatomic magnetic interactions, can be analytically extracted.

The total scalar spin chirality (χ) in the system can be calculated by the following formula:

$$\chi = \sum_{\langle ijk \rangle} \mathbf{S}_i \cdot (\mathbf{S}_j \times \mathbf{S}_k) \mathbf{n}_{ijk} \quad (5)$$

where \mathbf{S}_α ($\alpha = i, j, k$) is the spin at point α , \mathbf{n}_{ijk} is the unit direction vector of the triangle formed by sites i, j , and k , and the sum runs over all triangles $\langle ijk \rangle$ in each tetrahedron as shown in Fig. 1a.

We performed projected crystal orbital Hamiltonian population (pCOHP) analysis using the LOBSTER⁵⁵ code. This method, applied to the VASP-calculated wavefunctions with *spd* basis for Mn and *sp* basis for N, quantifies orbital-pair bonding strength via the integrated pCOHP (IpCOHP). It allowed us to directly compare the strain evolution of two competing interactions: the Mn3c-N orbital hybridization and the direct Mn3c-Mn3c orbital overlap.

Data Availability

All data generated or analyzed during this study are included in this published article.

Acknowledgement

The authors gratefully acknowledge the financial support provided by the National Natural Science Foundation of China (Grant No.~51971087), the "333 Talent Project" of Hebei Province (Grant No.~C20231105), the Basic Research Project of Shijiazhuang Municipal Universities in Hebei Province (Grant No.~241790617A), the Central Guidance on Local Science and Technology Development Fund of Hebei Province (Grant No.~236Z7606G), and the Science Foundation of Hebei Normal University (Grant No.~L2024B08). These funding sources have been instrumental in facilitating

the completion of this research.

Author Contributions

X.L. performed the first-principles calculations, analyzed the data, and wrote the original draft of the manuscript. L.M. conceived the idea, supervised the project, acquired the funding, and substantially revised the manuscript. M.Z. and S.N. assisted with the structural modeling and DFT calculations. Yu.L. and Ya.L. contributed to the data visualization and the analysis of magnetic exchange interactions. J.Z., Y.Z., and F.M. participated in the rigorous discussions regarding the bond-selective mechanism and scalar spin chirality. D.Z., G.L., C.Z., and D.H. provided technical support for the electronic structure analyses and contributed to the theoretical interpretation. All authors have read and approved the final manuscript.

Competing interests

All authors declare no financial or non-financial competing interests.

References

- 1 Taguchi, Y., Oohara, Y., Yoshizawa, H., Nagaosa, N. & Tokura, Y. Spin Chirality, Berry Phase, and Anomalous Hall Effect in a Frustrated Ferromagnet. *Science* **291**, 2573 (2001).
- 2 Takatsu, H., Yonezawa, S., Fujimoto, S. & Maeno, Y. Unconventional anomalous hall effect in the metallic triangular-lattice magnet PdCrO₂. *Phys. Rev. Lett.* **105**, 137201 (2010).
- 3 Takagi, H. *et al.* Spontaneous topological Hall effect induced by non-coplanar antiferromagnetic order in intercalated van der Waals materials. *Nat. Phys.* **19**, 961–968 (2023).
- 4 Sürgers, C., Fischer, G., Winkel, P. & Löhneysen, H. v. Large topological Hall effect in the non-collinear phase of an antiferromagnet. *Nat. Commun.* **5**, 3400 (2014).
- 5 Machida, Y., Nakatsuji, S., Onoda, S., Tayama, T. & Sakakibara, T. Time-reversal symmetry breaking and spontaneous Hall effect without magnetic dipole order. *Nature* **463**, 210-213 (2010).
- 6 Ueland, B. G. *et al.* Controllable chirality-induced geometrical Hall effect in a frustrated highly correlated metal. *Nat. Commun.* **3**, 1067 (2012).
- 7 Xu, S. *et al.* Universal scaling law for chiral antiferromagnetism. *Nat. Commun.* **15**, 3717 (2024).
- 8 Khanh, N. D. *et al.* Gapped nodal planes and large topological Nernst effect in the chiral lattice antiferromagnet CoNb₃S₆. *Nat. Commun.* **16**, 2654 (2025).

- 9 Oh, T. & Nagaosa, N. Phonon Thermal Hall Effect in Mott Insulators via Skew Scattering by the Scalar Spin Chirality. *Phys. Rev. X* **15**, 011036 (2025).
- 10 Kim, H. L. *et al.* Thermal Hall effects due to topological spin fluctuations in YMnO_3 . *Nat. Commun.* **15**, 243 (2024).
- 11 Song, J. *et al.* Higher harmonics in planar Hall effect induced by cluster magnetic multipoles. *Nat. Commun.* **13**, 6501 (2022).
- 12 Zhu, Y.-P. *et al.* Observation of plaid-like spin splitting in a noncoplanar antiferromagnet. *Nature* **626**, 523-528 (2024).
- 13 Baral, P. R. *et al.* Fluctuation-driven topological Hall effect in room-temperature itinerant helimagnet Fe_3Ga_4 . *Nat. Commun.* **16**, 3898 (2025).
- 14 Wang, W. *et al.* Spin chirality fluctuation in two-dimensional ferromagnets with perpendicular magnetic anisotropy. *Nat. Mater.* **18**, 1054-1059 (2019).
- 15 Li, X. *et al.* Momentum-space and real-space Berry curvatures in Mn_3Sn . *SciPost Phys.* **5**, 063 (2018).
- 16 Huang, D. *et al.* Multiple unconventional Hall effects induced by noncoplanar spin textures in SmMn_2Ge_2 . *Phys. Rev. B* **109**, 144406 (2024).
- 17 Martin, I. & Batista, C. D. Itinerant Electron-Driven Chiral Magnetic Ordering and Spontaneous Quantum Hall Effect in Triangular Lattice Models. *Phys. Rev. Lett.* **101**, 156402 (2008).
- 18 Kato, Y., Martin, I. & Batista, C. D. Stability of the spontaneous quantum Hall state in the triangular Kondo-lattice model. *Phys. Rev. Lett.* **105**, 266405 (2010).
- 19 Chern, G.-W. & Batista, C. D. Spontaneous Quantum Hall Effect via a Thermally Induced Quadratic Fermi Point. *Phys. Rev. Lett.* **109**, 156801 (2012).
- 20 Zhou, X., Feng, W., Li, Y. & Yao, Y. Spin-Chirality-Driven Quantum Anomalous and Quantum Topological Hall Effects in Chiral Magnets. *Nano Lett.* **23**, 5680-5687 (2023).
- 21 Zhou, J. *et al.* Predicted Quantum Topological Hall Effect and Noncoplanar Antiferromagnetism in $\text{K}_0.5\text{RhO}_2$. *Phys. Rev. Lett.* **116**, 256601 (2016).
- 22 Feng, W. *et al.* Topological magneto-optical effects and their quantization in noncoplanar antiferromagnets. *Nat. Commun.* **11**, 118 (2020).
- 23 Shindou, R. & Nagaosa, N. Orbital Ferromagnetism and Anomalous Hall Effect in Antiferromagnets on the Distorted fcc Lattice. *Phys. Rev. Lett.* **87**, 116801 (2001).
- 24 Reis, R. D. d. *et al.* Pressure tuning of the anomalous Hall effect in the chiral antiferromagnet Mn_3Ge . *Phys. Rev. Mater.* **4**, 051401(R) (2020).
- 25 Grohol, D. *et al.* Spin chirality on a two-dimensional frustrated lattice. *Nat. Mater.* **4**, 323-328 (2005).
- 26 Fujishiro, Y. *et al.* Giant anomalous Hall effect from spin-chirality scattering in a chiral magnet. *Nat. Commun.* **12**, 317 (2021).
- 27 Li, X., Koo, J., Zhu, Z., Behnia, K. & Yan, B. Field-linear anomalous Hall effect and Berry curvature induced by spin chirality in the kagome antiferromagnet Mn_3Sn . *Nat. Commun.* **14**, 1642 (2023).
- 28 Singh, C. *et al.* Higher order exchange driven noncoplanar magnetic state and large anomalous Hall effects in electron doped kagome magnet Mn_3Sn . *npj Quantum Mater.* **9**, 43 (2024).

- 29 Deng, S. *et al.* Controlling Chiral Spin States of a Triangular-Lattice Magnet by Cooling in a Magnetic Field. *Adv. Funct. Mater.* **29**, 1900947 (2019).
- 30 Shiomi, Y., Mochizuki, M., Kaneko, Y. & Tokura, Y. Hall effect of spin-chirality origin in a triangular-lattice helimagnet $\text{Fe}_{1.3}\text{Sb}$. *Phys. Rev. Lett.* **108**, 056601 (2012).
- 31 Ueda, K. *et al.* Topological Hall Effect in Pyrochlore Lattice with Varying Density of Spin Chirality. *Phys. Rev. Lett.* **108**, 156601 (2012).
- 32 Takei, W. J., Heikes, R. R. & Shirane, G. Magnetic Structure of Mn_4N -Type Compounds. *Phys. Rev.* **125**, 1893-1897 (1962).
- 33 Akagi, Y. & Motome, Y. Spin Chirality Ordering and Anomalous Hall Effect in the Ferromagnetic Kondo Lattice Model on a Triangular Lattice. *J. Phys. Soc. Jpn.* **79**, 083711 (2010).
- 34 Machida, Y. *et al.* Unconventional Anomalous Hall Effect Enhanced by a Noncoplanar Spin Texture in the Frustrated Kondo Lattice $\text{Pr}_2\text{Ir}_2\text{O}_7$. *Phys. Rev. Lett.* **98**, 057203 (2007).
- 35 Li, X. *et al.* Chiral domain walls of Mn_3Sn and their memory. *Nat. Commun.* **10**, 3021 (2019).
- 36 Hirschberger, M. *et al.* Topological Nernst Effect of the Two-Dimensional Skyrmion Lattice. *Phys. Rev. Lett.* **125**, 076602 (2020).
- 37 Isogami, S., Masuda, K. & Miura, Y. Contributions of magnetic structure and nitrogen to perpendicular magnetocrystalline anisotropy in antiperovskite $\epsilon\text{-Mn}_4\text{N}$. *Phys. Rev. Lett.* **4**, 014406 (2020).
- 38 He, Y. *et al.* Noncollinear ferrimagnetism and anomalous Hall effects in Mn_4N thin films. *Phys. Rev. B* **106**, L060409 (2022).
- 39 Bayaraa, T., Ivanov, V., Tan, L. Z. & Griffin, S. M. Intrinsic origin and enhancement of topological responses in ferrimagnetic antiperovskite Mn_4N . *Phys. Rev. B* **109**, 014430 (2024).
- 40 Tenasini, G. *et al.* Giant anomalous Hall effect in quasi-two-dimensional layered antiferromagnet $\text{Co}_{1/3}\text{NbS}_2$. *Phys. Rev. Res.* **2**, 023051 (2020).
- 41 Bayaraa, T., Xu, C. & Bellaiche, L. Magnetization Compensation Temperature and Frustration-Induced Topological Defects in Ferrimagnetic Antiperovskite Mn_4N . *Phys. Rev. Lett.* **127**, 217204 (2021).
- 42 Zhang, R., He, Y., Fruchart, D., Coey, J. M. D. & Gercsi, Z. Rare-earth-free noncollinear metallic ferrimagnets $\text{Mn}_{4-x}\text{Z}_x\text{N}$ with compensation at room temperature. *Acta Mater.* **234**, 118021 (2022).
- 43 Michael Uhl, S. F. M., and Peter Mohn. Ab initio analysis of magnetic properties in noncollinearly ordered Mn_4N . *Phys. Rev. B* **55**, 2995 (1997).
- 44 Adhikari, V. *et al.* First-principles study of mechanical and magnetic properties of transition metal (M) nitrides in the cubic M_4N structure. *J. Phys. Chem. Solids* **120**, 197-206 (2018).
- 45 Bloechl, R. D. a. P. E. Crystal orbital Hamilton populations (COHP): energy-resolved visualization of chemical bonding in solids based on density-functional calculations. *J. Phys. Chem.* **97**, 8617-8624 (1993).
- 46 Deringer, V. L., Tchougréeff, A. L. & Dronskowski, R. Crystal Orbital Hamilton Population (COHP) Analysis As Projected from Plane-Wave Basis Sets. *J. Phys. Chem. A* **115**, 5461-5466 (2011).

- 47 Goodenough, J. B. *Metals and Alloys in Magnetism and the Chemical Bond* (ed. Goodenough, J. B.) 321 (Interscience Publishers, 1963).
- 48 Cui, J. *et al.* Manipulation of magnetic structures and pressure-induced strong correlation properties in the frustrated Mn_3GaN antiperovskite. *Phys. Rev. B* **110**, 094438 (2024).
- 49 Kobayashi, M. & Mochizuki, M. Theory of magnetism-driven negative thermal expansion in inverse perovskite antiferromagnets. *Phys. Rev. Mater.* **3**, 024407 (2019).
- 50 D Fruchart, D. G., P Convert, P l'Heritier and J P Senateur. The non-collinear component in the magnetic structure of Mn_4N . *J. Phys. F: Met. Phys.* **9**, 2431 (1979).
- 51 Kresse, G. & Hafner, J. Ab initio molecular dynamics for liquid metals. *Phys. Rev. B* **47**, 558-561 (1993).
- 52 Kresse, G. & Furthmuller, J. Efficiency of ab-initio total energy calculations for metals and semiconductors using a plane-wave basis set. *Comput. Mater. Sci.* **6**, 15-50 (1996).
- 53 Kresse, G. & Furthmuller, J. Efficient iterative schemes for ab initio total-energy calculations using a plane-wave basis set. *Phys. Rev. B* **54**, 11169 (1996).
- 54 Xiang, H. J., Kan, E. J., Wei, S.-H., Whangbo, M. H. & Gong, X. G. Predicting the spin-lattice order of frustrated systems from first principles. *Phys. Rev. B* **84**, 224429 (2011).
- 55 Szasz, A., Motruk, J., Zaletel, M. P. & Moore, J. E. Chiral Spin Liquid Phase of the Triangular Lattice Hubbard Model: A Density Matrix Renormalization Group Study. *Phys. Rev. X* **10**, 021042 (2020).

Figure Legends

Figure 1 **Strain-induced magnetic phase transition and the emergence of scalar spin chirality order in Mn_4N .** **a** Magnetic and crystal structures of Mn_4N . There are only two types of magnetic tetrahedra in the lattice: red and blue. The green and red arrows represent the spin direction in the lattice and the direction of the total scalar spin chirality χ in each tetrahedron, respectively. **b** Schematic of a single tetrahedron of Mn atoms, which consists of four spin vectors \mathbf{S}_α ($\alpha = 1, 2, 3, 4$). Here $\alpha = 1$ and $\alpha = 2, 3, 4$ indicate the corresponding spin orientation \mathbf{S}_α at the Mn1a site and the Mn3c site, respectively. θ is the angle between the spins of the Mn1a site and the Mn3c site. **c** Energy dependence on strain at $\theta = 110^\circ$ and $\theta = 180^\circ$. **d** Dependence of χ and θ on strain under the magnetic ground state. **e** Schematic of the χ distribution between adjacent (111) lattice planes. The gray planes represent the

(111) lattice planes.

Figure 2. **Explore the requirements for the formation of scalar spin chiral order on local moments and exchange interactions.** **a** Strain dependence of the Mn moments at Mn1a and Mn3c sites. **b** Strain evolution of the Mn3c moment components: $Mn3c_{||[111]}$ (parallel to [111] crystal direction) and $Mn3c_{||(111)}$ (lying within the (111) lattice planes), corresponding to the blue and red arrow illustrated in the inset of **(c)**, respectively. **c** Strain variation of the nearest-neighbor exchange coupling constant J between Mn3c sites. Projected density of states (PDOS) of the Mn3c $3d$ orbitals onto the (111) plane at strains of -1.33% **(d)** and 3.00% **(e)**.

Figure 3. **Two key orbital bonding between nearest-neighbor Mn3c sites in Mn₄N through charge density difference (CDD) analysis.** CDD on the (001) lattice plane (corresponding to the red plane in Fig. 1a) under strains of -1.33% **(a)**, 0.53% **(b)**, and 2.66% **(c)**. The red and blue areas represent electron accumulation and depletion, respectively. The isosurface levels are set to $-0.028 e/\text{\AA}^3$ (red, positive) and $-0.06 e/\text{\AA}^3$ (blue, negative). Black dashed lines indicate charge contour levels. The red and blue dashed loops delineate the projections of the Mn3c and N orbitals onto the (001) plane, serving as spatial references for orbital hybridization. Schematic representations of the two orbital bonding configurations deduced from the CDD maps. Schematics of the polar σ covalent bond formed by the hybridization of the Mn3c $d_{3x^2-r^2}$ ($d_{3y^2-r^2}$) orbital and the N p_x (p_y) orbital **(d)** and the nonpolar σ covalent bond between the d_{xy} orbitals of nearest-neighbor Mn3c atoms **(e)**.

Figure 4. **Formation mechanism of the scalar spin chirality order via the**

quantitative orbital-resolved bonding analysis. Projected crystal orbital Hamiltonian population (pCOHP) profiles for the two principal orbital interactions: the Mn3c $d_{3x^2-r^2}$ and N p_x bond (red curves), and the Mn3c d_{xy} and Mn3c d_{xy} bond (blue curves) under strains of -1.33% (a), 0.53% (b), and 2.66% (c). Positive and negative $-pCOHP$ values denote bonding and antibonding characteristics, respectively. The red and blue text in each panel gives the integrated pCOHP (IpCOHP) values up to the Fermi level (measure of bond strength) of the Mn3c-N bond and the Mn3c-Mn3c bond, respectively. **d** Strain-dependent schematic of the dual modulation of the Mn3c || (111) moment and exchange interactions via bond-selective suppression. The left and right panels correspond to the covalent bond between the Mn3c $d_{3x^2-r^2}$ orbital and the N p_x orbital and the magnetic configuration under the compressive and tensile strain conditions, respectively. The green arrows denote the activated Mn3c || (111) moments. J_{FM} represents the nitrogen-mediated ferromagnetic superexchange interaction of the nearest-neighbor Mn3c via the Mn3c ($d_{3x^2-r^2}$)-N (p_x) covalent bond.